



Thermal reaction characterization of nano-aluminum powder at different heating rates by synchronous thermal analysis

Jiao Qu^{1,2} · Jun Deng^{1,3} · Zhen-Min Luo^{1,3} · Yang Xiao^{1,3} · Chi-Min Shu⁴

Received: 28 June 2022 / Accepted: 12 December 2022 / Published online: 16 January 2023
© Akadémiai Kiadó, Budapest, Hungary 2023

Abstract

This article reports an investigation on the thermal reactivity of nano-aluminum powder (NAP) in the air. We performed tests on the metallic powder in synchronous thermal analysis at four heating rates of 5, 10, 15, and 20 °C min⁻¹. Given the polymorphic phase change of aluminum, the oxidation process of NAP was divided into four stages. The results showed a notable effect from the heating rate on the oxidation of NAP. The mass gain decreased at stage II and increased at stage IV as the rate of heating increased. The maximum mass gain rate at 5, 10, 15, and 20 °C min⁻¹ was 2.38, 4.70, 33.79, and 53.38% min⁻¹, respectively, while the thermal release was 35,126, 27,955, 15,608, and 16,336 J g⁻¹, respectively. Furthermore, the average apparent activation energy, preexponential factor, and mechanism function were obtained by the kinetic integral method.

Keywords Thermal reactivity · Metallic powder · Polymorphic phase change · Maximum mass gain rate · Thermal release

Introduction

As a typical metallic powder, nano-aluminum powder (NAP) is substantially used in the top grade metal pigment and also has been widely applied in aerospace, chemical, metallurgy, and military industries [1, 2]. It has not only the properties of metallic aluminum powders but also the features of nanosized particles, such as small particle size, high Brunauer–Emmett–Teller specific surface area, and high surface energy. Thus, it also exhibits a significant potential risk

of being inflammable and explosive. Dust explosion accidents are prone to occur frequently, endangering human life and causing economic losses [3–5]. Therefore, an improved understanding of NAP explosions is vital for the prevention and control of industrial disasters in production, storage, transportation, and usage and has practical significance for the protection of life and possessions.

Numerous studies have focused on the explosion, ignition, combustion, and thermal analyzes of aluminum powder. Li et al. [6] analyzed the explosion characteristics of NAP-air mixtures in 20 L spherical vessels. Bernard et al. [7] delved into the ignition and explosibility of aluminum alloys applied in additive layer manufacturing. Wu et al. [8, 9] investigated the dust explosion characteristics of agglomerated 35 and 100 nm aluminum particles. By using a 20 L Siwek sphere, Denkevits et al. [10] revealed hybrid H₂/Al dust explosion characteristics. Liu et al. [11] and Zhang et al. [12] analyzed the effect of turbulence on aluminum dust explosions. Castellanos et al. [13] explored the effect of particle size dispersion on the explosive properties of aluminum powder. These studies have mainly focused on the explosion characteristics of aluminum powder, namely the maximum explosion pressure (P_{max}), the maximum rate of pressure rise $(dP/dt)_{max}$, and the minimum explosion concentration (MEC).

Studies on ignition and combustion have been strictly dedicated to influencing factors, such as particle size and

✉ Jiao Qu
jqqu2020@xust.edu.cn

✉ Yang Xiao
xiaoy@xust.edu.cn

¹ School of Safety Science and Engineering, Xi'an University of Science and Technology, No. 58, Yanta Mid. Rd., Xi'an 710054, Shaanxi, People's Republic of China

² Postdoctoral Program, Xi'an University of Science and Technology, No. 58, Yanta Mid. Rd., Xi'an 710054, Shaanxi, People's Republic of China

³ Shaanxi Key Laboratory of Prevention and Control of Coal Fire, No. 58, Yanta Mid. Rd., Xi'an 710054, Shaanxi, People's Republic of China

⁴ Graduate School of Engineering Science and Technology, National Yunlin University of Science & Technology, 123, University Rd., Sec. 3, Douliou 64002, Yunlin, Taiwan ROC

oxygen concentration. Huang et al. [14] investigated the combustion of bimodal nano- and micron-sized aluminum particle dusts in the air. Yuasa et al. [15] studied the ignition and combustion of aluminum in carbon dioxide streams. Bidabadi et al. [16] analyzed the effects of size distribution and ignition temperature on flame speeds in aluminum dust clouds. Zhu et al. [17] and Li et al. [18] analyzed the effects of oxygen concentration on combustion of aluminum. Gao et al. [19] investigated the flame propagation of 40 nm aluminum dust clouds by high-speed photography.

Some studies on the characteristics of aluminum powder thermal reaction in different environments have been conducted. Qu et al. [20] carried out the research on the thermal reaction characteristics and microstructure evolution of aluminum nanopowder in various mixtures of oxygen and nitrogen atmosphere. Tseng et al. [21] researched the thermal reaction characteristics of metal nanopowders by using differential scanning calorimetry (DSC). Zhu et al. [22] investigated the thermal reaction characteristics of micron-sized aluminum powders in CO₂ by using synchronous thermal analysis (STA) and analyzed the effect of heating rates. Johnson et al. [23] conducted an experimental investigation of the thermal reaction characteristics of the 30–500 nm aluminum powder in the air, oxygen, and nitrogen by using thermogravimetric (TG) analysis. Vlaskin et al. [24] demonstrated the oxidation kinetics of the micron-sized aluminum powder in high-temperature boiling water.

Profound theoretical and experimental investigations have been conducted for aluminum powders, particularly the micro-sized powder. However, few reports have analyzed the oxidation kinetics of NAP and the effects of heating rates. Recently, the characteristics and mechanisms of NAP at different heating rates were studied by using STA, based on thermal reaction kinetics. The results can provide theoretical support for the ignition and combustion of NAP.

Experimental method

Sample

The NAP was characterized by high purity, high sphericity, less impurity, and high activated aluminum content. The sample used in these experiments was from Chaowei Nanotechnology, Inc. (Shanghai, PR China), and its purity was greater than 99.9%. It was prepared by changing current, laser ion beam and gas phase method. In this study, the nominal particle size of aluminum powder was 100 nm. In order to avoid the influence of wetting and agglomeration in the process of experiments, the NAP was stored in a dry and dark vacuum environment, under the protection of inert gases for antistatic packaging.

By using analytical reagent (AR) anhydrous alcohol as the dispersion agent, the particle size distribution of NAP was determined using Mastersizer 2000 laser particle size analysis (Malvern, UK) after ultrasonic dispersion. The microstructure of NAP was identified with JSM-6460 scanning electron microscope (SEM) at 20.00 kV acceleration voltage, 5.9 mm working distance, and 200 KX magnification. The particle size distribution and SEM are presented in Fig. 1. The granulometric properties are given in Table 1.

Specific surface area is a crucial index to evaluate the physical and chemical properties of NAP. It has an apparent influence on thermal properties and chemical stability. As presented in Table 1, the specific surface area of NAP was ca. 36.4 m² g⁻¹. The median particle size was 0.168 μm.

As shown SEM image, the aluminium particles were approximately spherical. This is because the cohesion of the particles (electrostatic, Van der Waals, and Coulomb forces) had an important effect on the agglomeration of NAP [25]. If the agglomeration is severe, certain chemical or mechanical energy can be utilized to eliminate the agglomeration [26]. However, the instantaneous agglomeration is unavoidable when the dust explosion actually occurs. Therefore, the agglomeration of NAP was not eliminated in this study.

Experiments

The tests were performed on an STA 449 F3 simultaneous thermal analyzer (STA, Netzsch, Germany), which could simultaneously measure the mass change and heat release rate. The schematic diagram of STA mainly included the intake and exhaust system, the weighing system, the heating furnace, and the data collection system, as shown in Fig. 2. The intake system consisted of three channels. N₂ was used as a protection gas. In addition, O₂ and N₂ were applied as two-way purge gases. The electric furnace heating, water

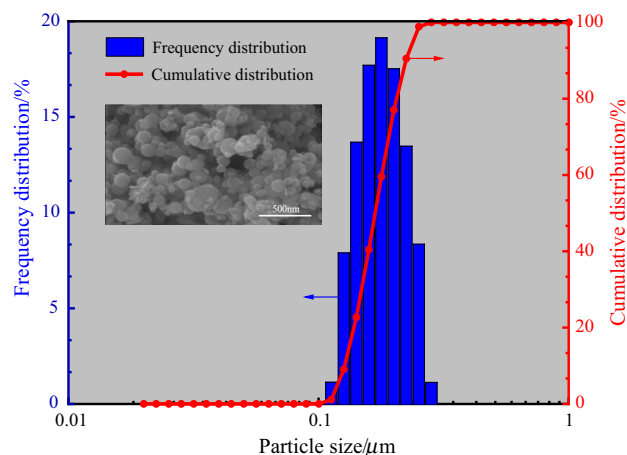


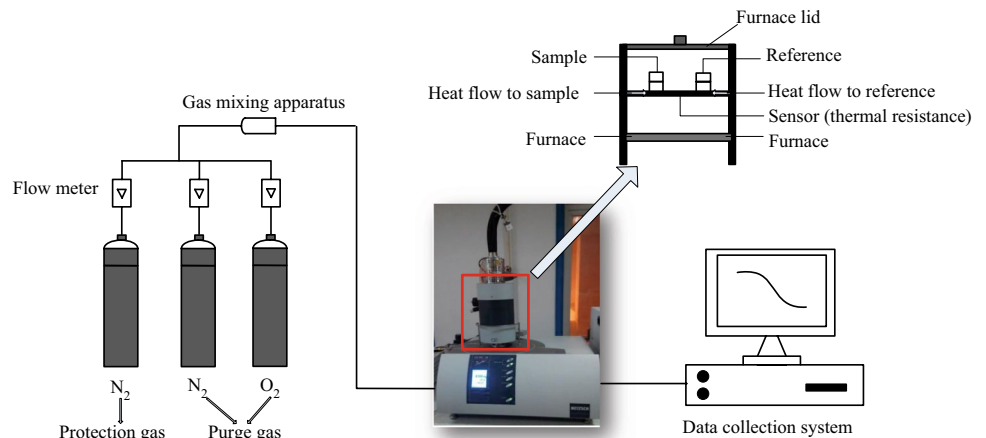
Fig. 1 Particle size distribution and SEM of NAP

Table 1 Granulometric properties of NAP

$S_v/m^2\ g^{-1}$	$d(3,2)/\mu m$	$d(4,3)/\mu m$	$d_{10}/\mu m$	$d_{50}/\mu m$	$d_{90}/\mu m$	σ
36.4	0.165	0.172	0.127	0.168	0.223	0.57

S_v is the specific surface area, $m^2\ g^{-1}$; $d(3,2)$ is the surface area mean particle size, μm ; $d(4,3)$ is the volume average diameter, μm ; d_{50} is the corresponding particle size when the cumulative distribution reaches 50%, also called the median particle size, μm ; σ is the particle diameter distribution width, $\sigma = (d_{90} - d_{10})/d_{50}$

Fig. 2 Simultaneous thermal analyzer



circulation cooling. The maximum heating temperature is 1000 °C.

In order to ensure adequate reaction of the sample, the mass of sample was $5.0 \pm 0.1\ mg$ and the flow rate of the gas supply volume was $100\ mL\ min^{-1}$. The tests were performed in ambient air under the conditions with 5, 10, 15, and $20\ ^\circ C\ min^{-1}$ from 30 to 1000 °C. TG, DTG, and DSC measurements were obtained.

Kinetic integral method

Satava-Sestak method

Differential expression of the first type of dynamic equations for thermal analysis, as shown in Eq. 1:

$$\frac{d\alpha}{dT} = \frac{A}{\beta} f(\alpha) \exp\left(-\frac{E}{RT}\right) \tag{1}$$

Considering that the initial reaction temperature is low, the two sides of Eq. 1 can be integrated in the range of 0- α and 0-T, Eq. 2 can be obtained:

$$\int_0^\alpha \frac{d\alpha}{f(\alpha)} = G(\alpha) = \frac{A}{\beta} \int_0^T \exp\left(-\frac{E}{RT}\right) dT \tag{2}$$

In Eq. 2, $\int_{T_0}^T \exp(-E/RT)dT$ is Boltzmann factor integral. It has no analytical solution, and we can solve the approximate solution.

Let $u = E/RT$, then $T = E/Ru$. Logarithm on both sides of the equation as shown in Eq. 3:

$$dT = -\frac{E}{Ru^2} du \tag{3}$$

Equation 3 is substituted into Eqs. 2, 4 is obtained:

$$G(\alpha) = \frac{AE}{\beta R} P(u) \tag{4}$$

where $P(u)$ is expressed as Eq. 5.

$$P(u) = \int_\infty^u \frac{-e^{-u}}{u^2} du \tag{5}$$

and

$$\log P(u) = -2.315 - 0.4567 \frac{E}{RT} \tag{6}$$

Taking the logarithm of the two sides of Eq. 4, combining with Eq. 6, Satava-Sestak equation can be obtained, as shown in Eq. 7.

$$\log G(\alpha) = \log \frac{AE_s}{R\beta} - 2.315 - 0.4567 \frac{E_s}{RT} \tag{7}$$

In these equations, α is the conversion rate of aluminum powder during thermal oxidation at time t, %; $f(\alpha)$ is the differential mechanism function; $G(\alpha)$ is the integral mechanism function; E_s is apparent activation energy by Satava-Sestak

method, J mol^{-1} ; A is the pre-exponential factor, min^{-1} ; β is the heating rate, $^{\circ}\text{C min}^{-1}$; R is a universal gas constant, $8.314 \text{ J mol}^{-1} \text{ K}^{-1}$; and T is the reaction temperature, $^{\circ}\text{C}$.

Metal particles usually undergo heterogeneous gas–solid reaction during oxidation. The gas–solid reaction modes mainly include Jander, Shrinking global (volume), and Shrinking cylinder (area) [27]. The corresponding Integral mechanism functions $G(\alpha)$ were derived from mechanism functions, as described in Table 2.

With a fixed heating rate, $\log(AE_s/R\beta)$ is a constant. Equation 7 becomes a linear equation.

Let $Y = \log G(\alpha)$, $X = 1/T$, $a = -0.4567(E_s/R)$, $b = \log(AE_s/R\beta) - 2.315$, and Eq. 7 can be expressed by Eq. 8:

$$Y = aX + b \quad (8)$$

Ozawa method

Ozawa formula is obtained by Eqs. 4 and 6, as expressed by Eq. 9.

$$\log \beta = \log\left(\frac{AE_o}{RG(\alpha)}\right) - 2.315 - 0.4567 \frac{E_o}{RT} \quad (9)$$

where E_o is apparent activation energy by Ozawa method.

Let $Z = \log \beta$, $X = 1/T$, $c = -0.4567(E_o/R)$, $d = \log\left(\frac{AE_o}{RG(\alpha)}\right) - 2.315$, therefore Eq. 9 can be expressed by Eq. 10:

$$Z = cX + d \quad (10)$$

Results and discussion

Thermal oxidation characteristics

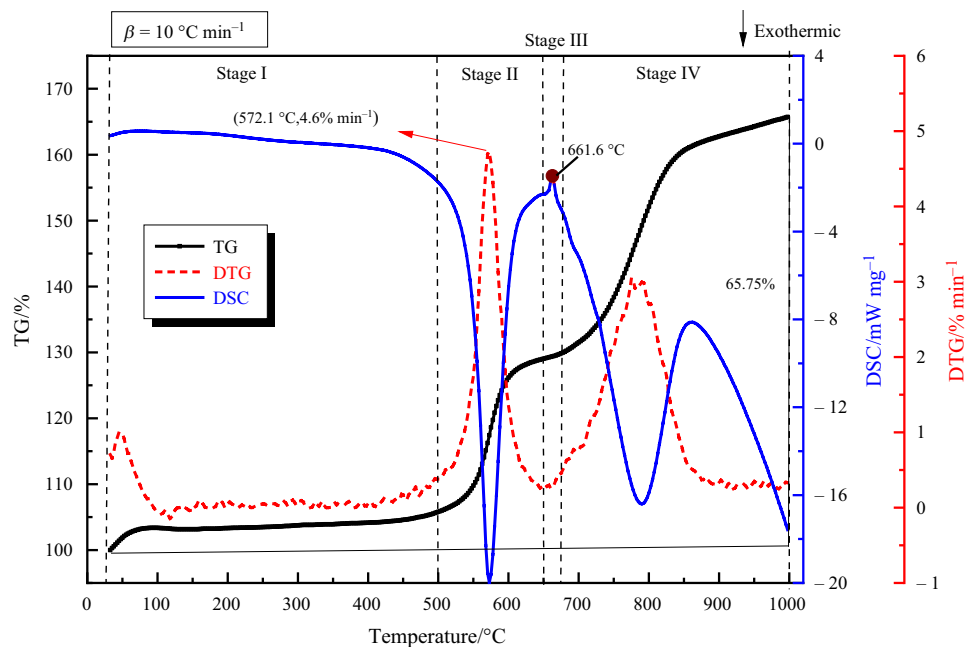
The TG-DTG-DSC curves of NAP at a heating rate of $10^{\circ}\text{C min}^{-1}$ are depicted in Fig. 3. A small endothermic peak presented at 661.6°C , which was near the melting point of aluminum at 660°C . Considerable exothermic peaks also presented at 572.7 and 789.9°C . With the increase of temperature, the TG curve gradually increased, and the mass of aluminum powder continued to increase [23]. DTG and DSC indicated a bimodal curve with increasing temperature. The oxidation rate and releasing heat changed periodically. Therefore, the dynamic oxidation process of NAP can be divided into four stages, which are as follows:

At stage I, the initial stage of oxidation, the temperature was $30\text{--}500^{\circ}\text{C}$ and the TG and DTG curves changed slightly while the DSC curve did not exhibit obvious endothermic or exothermic peaks. The sample exhibited a small increment of only 5.78%. Oxidation was difficult, and the oxidation rate was low under 500°C . At the initial stage of oxidation, the oxidation products of NAP were mainly amorphous alumina.

At stage II, the drastic oxygenation stage, the temperature was in the range of $500\text{--}650^{\circ}\text{C}$, the TG curve exhibited an apparent rise, and the sample indicated a significant mass gain of approximately 23.24%. Shown as a DTG curve, the oxidation rate increased during $500\text{--}650^{\circ}\text{C}$. The DSC curve appeared narrow and presented a sharp exothermic peak. At this stage, the oxidation products of NAP changed from amorphous alumina to $\gamma\text{-Al}_2\text{O}_3$. When the $\gamma\text{-Al}_2\text{O}_3$ did not form a continual full enclosure on the surface of the aluminum particle, the exposed aluminum

Table 2 Mechanism functions adapted for heterogeneous gas–solid reaction

No	Equations	Mechanism	Integral $G(\alpha)$	Differential $f(\alpha)$
3	Jander	Two-dimensional diffusion, $n = 1/2$	$\left[1 - (1 - \alpha)^{1/2}\right]^{1/2}$	$4(1 - \alpha)^{1/2} \left[1 - (1 - \alpha)^{1/2}\right]^{1/2}$
4	Jander	Two-dimensional diffusion, $n = 1/2$	$\left[1 - (1 - \alpha)^{1/2}\right]^{1/2}$	$(1 - \alpha)^{1/2} \left[1 - (1 - \alpha)^{1/2}\right]^{-1}$
5	Jander	Three-dimensional diffusion, $n = 1/2$	$\left[1 - (1 - \alpha)^{1/3}\right]^{1/2}$	$6(1 - \alpha)^{2/3} \left[1 - (1 - \alpha)^{1/3}\right]^{1/2}$
6	Jander	Three-dimensional diffusion, global symmetry, $n = 2$	$\left[1 - (1 - \alpha)^{1/3}\right]^2$	$\frac{3}{2}(1 - \alpha)^{2/3} \left[1 - (1 - \alpha)^{1/3}\right]^{-1}$
29	Shrinking global (volume)	Phase boundary reaction, global symmetry, R_3 , deceleration $\alpha - t$, $n = 1/3$	$1 - (1 - \alpha)^{1/3}$	$3(1 - \alpha)^{2/3}$
30	Shrinking global (volume)	$n = 3$ (3D)	$3 \left[1 - (1 - \alpha)^{1/3}\right]$	$(1 - \alpha)^{2/3}$
31	Shrinking cylinder (area)	Phase boundary reaction, cylinder symmetry, R_2 , deceleration $\alpha - t$, $n = 1/2$	$1 - (1 - \alpha)^{1/2}$	$2(1 - \alpha)^{1/2}$
32	Shrinking cylinder (area)	$n = 2$ (2D)	$2 \left[1 - (1 - \alpha)^{1/2}\right]$	$(1 - \alpha)^{1/2}$

Fig. 3 TG-DTG-DSC curves of NAP at $10\text{ }^{\circ}\text{C min}^{-1}$ 

directly contacted with the air, which caused the oxidation rate to increase rapidly. If $\gamma\text{-Al}_2\text{O}_3$ fully covered the aluminum particle, the oxidation rate was promptly reduced [28].

At stage III, the solid aluminum melting stage, the temperature ranged from 650 to 670 $^{\circ}\text{C}$, and the TG curve rose slowly. The sample exhibited a slight mass gain of only 0.6%. A brief and weak exothermic peak appeared in the DSC curve located at approximately 660 $^{\circ}\text{C}$, which corresponded to the melting of the aluminum core of the particle, as proposed in [29]. The aluminum powder melted and absorbed heat while the oxidation reaction released heat. The two reactions proceeded simultaneously but alone. These two reactions offset each other; thus, the exothermic effect was not noteworthy [30].

At stage IV, the secondary oxidation stage, the temperature was 670–1000 $^{\circ}\text{C}$, TG curve rose again, and the sample exhibited a notable gain of 36.13%. The DTG curve also increased considerably. The sample again revealed accelerated oxidation, and an exothermic peak appeared in the DSC curve. During this stage, aluminum oxide changed from $\gamma\text{-Al}_2\text{O}_3$ to $\alpha\text{-Al}_2\text{O}_3$, which led to the shrinking surface area. In addition, molten aluminum expanded when heated. Consequently, the surface of the oxidized shell was cracked or broken, activated aluminum was released, and oxidation reaction reoccurred [31].

As the temperature increased more than 1000 $^{\circ}\text{C}$, the TG curve continued to rise. With continuous heating, the oxidation reaction also continuously proceeded. The academics [32] noted that aluminum powder could not be completely oxidized in the oxidation process because dense alumina was formed on the surface [32, 33].

The TG-DTG-DSC curves of NAP at heating rates of 5, 15, and 20 $^{\circ}\text{C min}^{-1}$ are depicted in Figs. 4, 5 and 6. In addition, the oxidation process of aluminum powder followed four stages at heating rates of 5, 15, and 20 $^{\circ}\text{C min}^{-1}$.

Ignition temperature is a vital reference index to describe the combustion properties of combustible materials [34]. The sample started to burn at the ignition temperature T_i . T_i is determined by identifying the tangent line of the temperature point on the TG curve corresponding to the maximum thermal mass gain rate; that is, the tangent line of the intersection point of the TG curve and the vertical line of the maximum peak of the DTG curve [35].

When the heating rate was 20 $^{\circ}\text{C min}^{-1}$: the mass gain of the aluminum powder Δm was 51.56%. The ignition temperature, the DTG peak temperature T_p , and the melting temperature T_m was 481.75, 573.7, and 665.7 $^{\circ}\text{C}$, respectively. The average rate of mass gain $DTG|_{\text{mean}}$, and the maximum rate of mass gain $DTG|_{\text{max}}$ was 1.37% min^{-1} and 53.38% min^{-1} , correspondingly. The thermal oxidation parameters of the NAP at multiple heating rates are listed in Table 3.

Effects of heating rates on thermal oxidation characteristics

The TG, DTG, and DSC curves of NAP were analyzed at multiple heating rates, as shown in Figs. 7–11. Figure 7 presents the relationship between the mass gain of NAP and temperature at multiple heating rates, which demonstrates the mass change at the four stages at a heating rate of 5 $^{\circ}\text{C min}^{-1}$. The mass change of NAP at different stages with various heating rates is given in Table 4. As the heating rate increased, the mass gain at stage I barely changed:

Fig. 4 TG-DTG-DSC curves of NAP at $5\text{ }^{\circ}\text{C min}^{-1}$

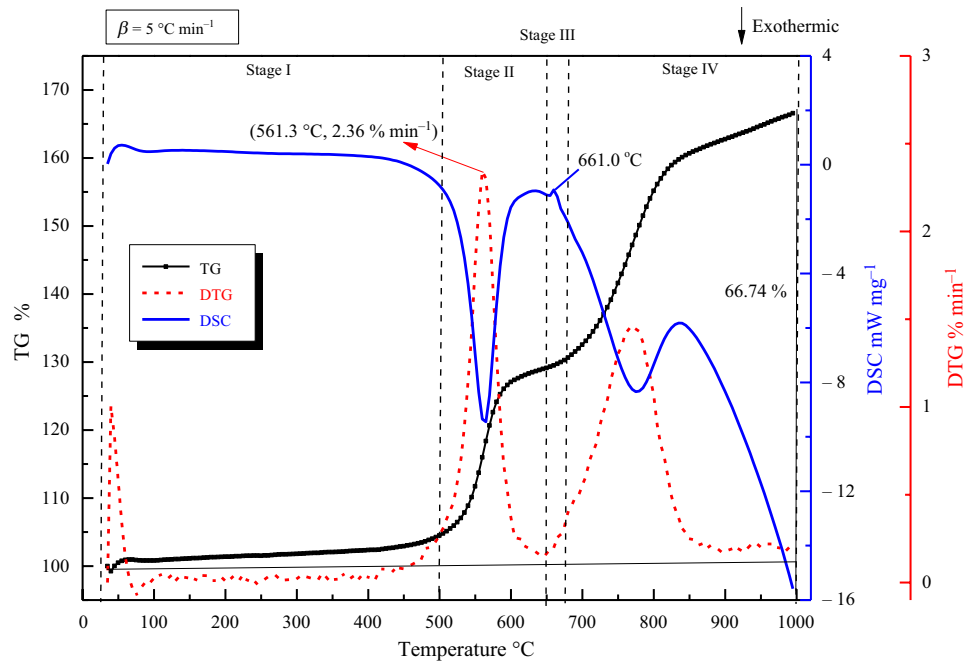
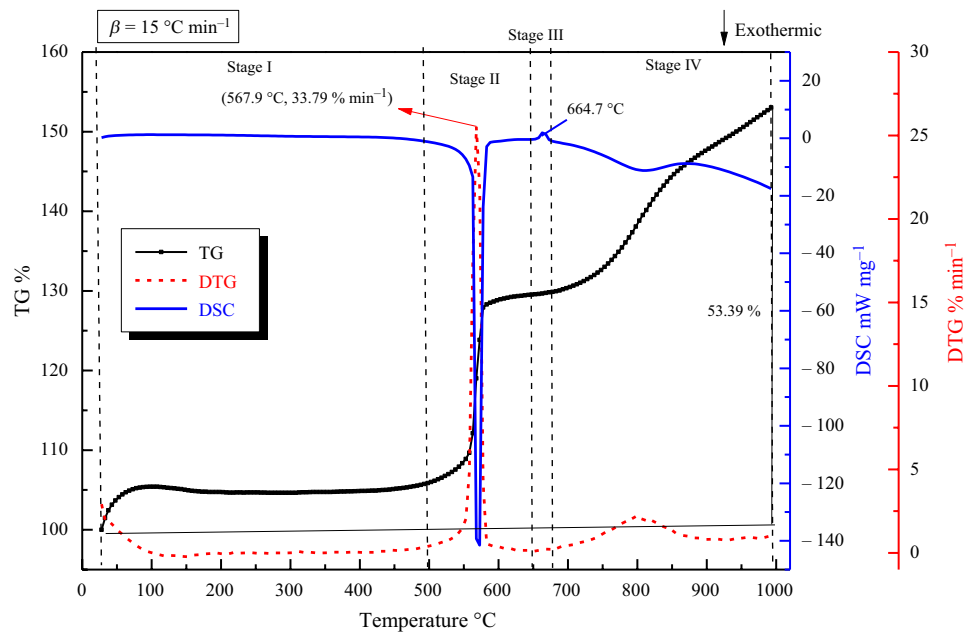


Fig. 5 TG-DTG-DSC curves of NAP at $15\text{ }^{\circ}\text{C min}^{-1}$



$\Delta m_1 = 4.5\% - 6.17\%$. The heating rate had little effect on the mass gain of the NAP at the initial oxidation because the aluminum powder was readily oxidized in the air. A thin oxidation film, namely amorphous alumina, was formed and attached to the surface of the aluminum particle. As the temperature increased, the oxidation film thickened. The oxidation film did not thicken further after the amorphous alumina became relatively stable. The critical thickness of the amorphous alumina was approximately 4 nm [36, 37].

During stage II, the mass gain at the higher heating rates (15 and $20\text{ }^{\circ}\text{C min}^{-1}$) was considerably greater than that at the lower heating rates (5 and $10\text{ }^{\circ}\text{C min}^{-1}$) because the surface area shrank during the transition from amorphous alumina to $\gamma\text{-Al}_2\text{O}_3$, causing cracks in the shell. With an increase in the heating rate, the transition from amorphous aluminum to $\gamma\text{-Al}_2\text{O}_3$ accelerated, then the surface area shrank severely and caused the increasing number of cracks in the shell. As a result, the oxidation degree deepened.

Fig. 6 TG-DTG-DSC curves of NAP at 20 °C min⁻¹

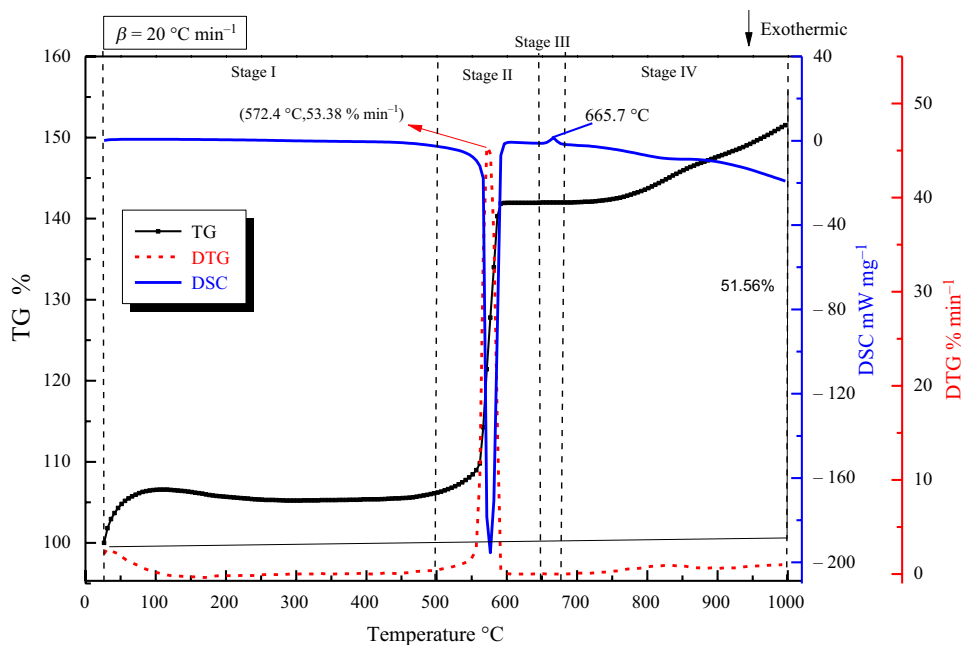


Table 3 Thermal oxidation characteristic parameters of NAP at multiple heating rates

$\beta/^\circ\text{C min}^{-1}$	$\Delta m/\%$	$T_i/^\circ\text{C}$	$T_p/^\circ\text{C}$	$T_m/^\circ\text{C}$	$DTG _{\text{mean}}/\% \text{ min}^{-1}$	$DTG _{\text{max}}/\% \text{ min}^{-1}$
5	66.74	311.96	561.3	661	0.29	2.38
10	65.75	317.41	572.0	661.6	0.68	4.7
15	53.39	434.06	567.9	664.7	0.95	33.79
20	51.56	481.75	572.4	665.7	1.37	53.38

Fig. 7 TG curves of NAP at the multiple heating rates

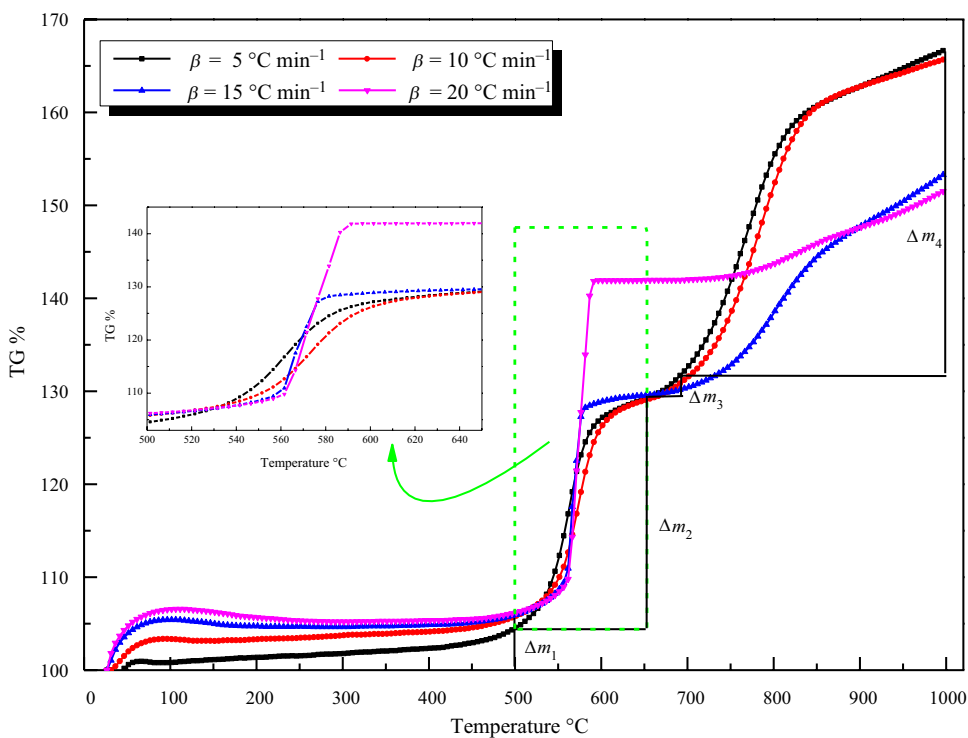
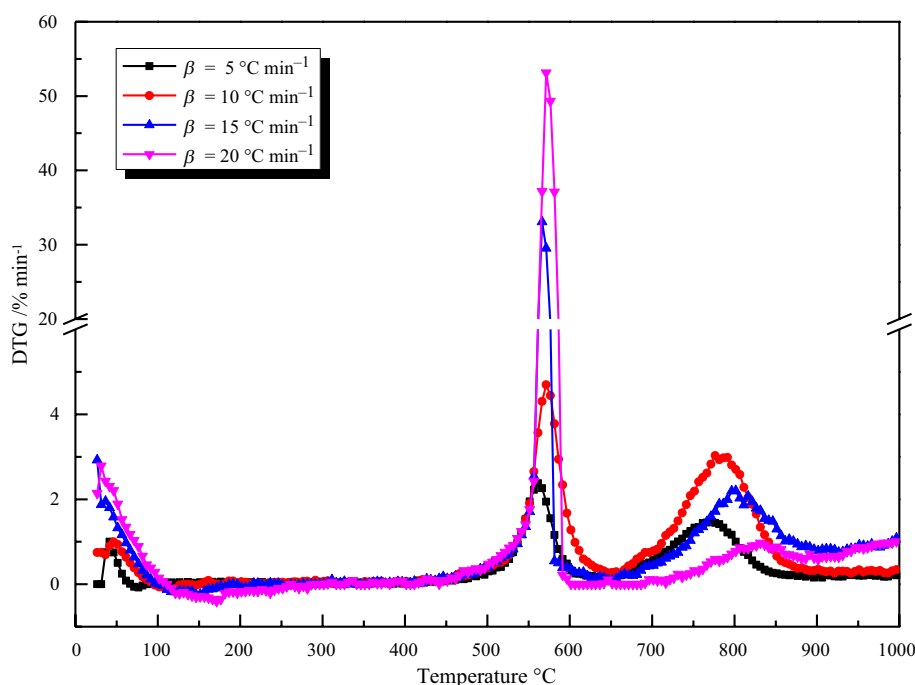


Fig. 8 DTG bimodal curves of NAP at multiple heating rates



Therefore, the mass gain of the aluminum powder increased [38, 39].

During stage III, as the heating rate increased, the mass barely changed at the beginning and then later decreased. Even when the heating rate was 20 °C min^{-1} , the mass change was 0%. The melting endotherm and the oxidative exotherm of the NAP interacted, and the mass loss and mass gain of the aluminum powder offsetted each other [30].

During stage IV, the process of aluminum powder oxidation was mainly due to the transformation from $\gamma\text{-Al}_2\text{O}_3$ to $\alpha\text{-Al}_2\text{O}_3$. The mass gain at the lower heating rate was notably greater than the higher heating rate. Based on our analysis, the aluminum powder was oxidized by a diffusion layer at a lower heating rate. The oxidation reaction reached a higher

degree of completion. As shown in Table 3, within the temperature range of 30–1000 °C, the lower the heating rate, the greater the mass gain Δm . At multiple heating rates, a bimodal appeared in all the DTG curves. With the increase in temperature, the aluminum powder underwent secondary oxidation (Fig. 8).

Based on Table 3 and Fig. 9, the value of the DTG's first peak rapidly increased from 2.38 % min^{-1} at 5 °C min^{-1} and 4.7 % min^{-1} at 10 °C min^{-1} to 33.79 % min^{-1} at 15 °C min^{-1} and 53.38 % min^{-1} at 20 °C min^{-1} , increased by 97.48, 618.93, and 57.96%, respectively. The heating rate notably affected the value of the first peak. When the amorphous alumina was converted into to $\gamma\text{-Al}_2\text{O}_3$, the greater the heating rate was, the higher the oxidation rate

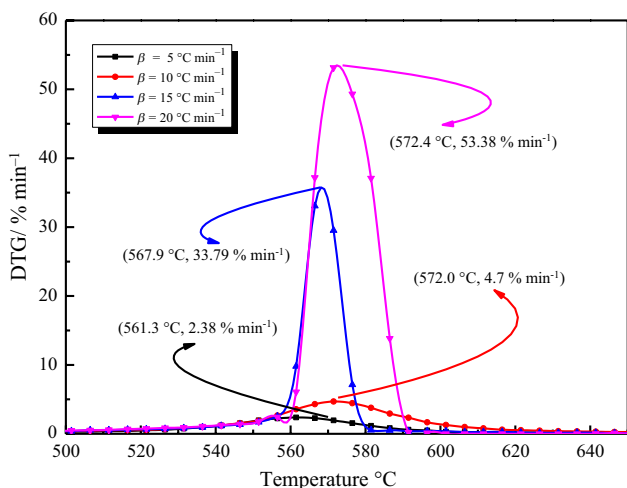


Fig. 9 DTG first-peak curves of NAP at stage II

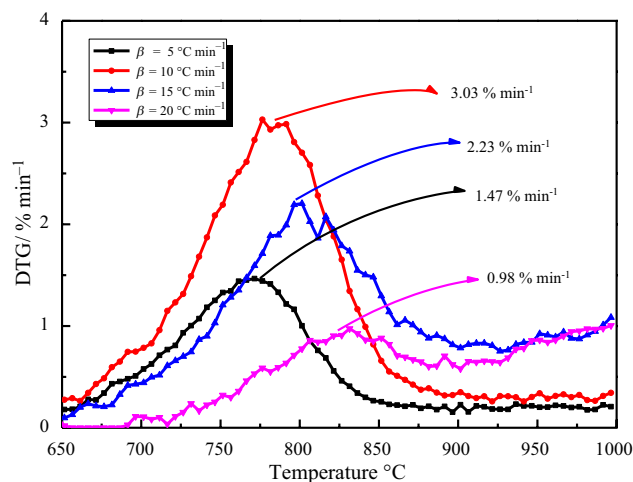
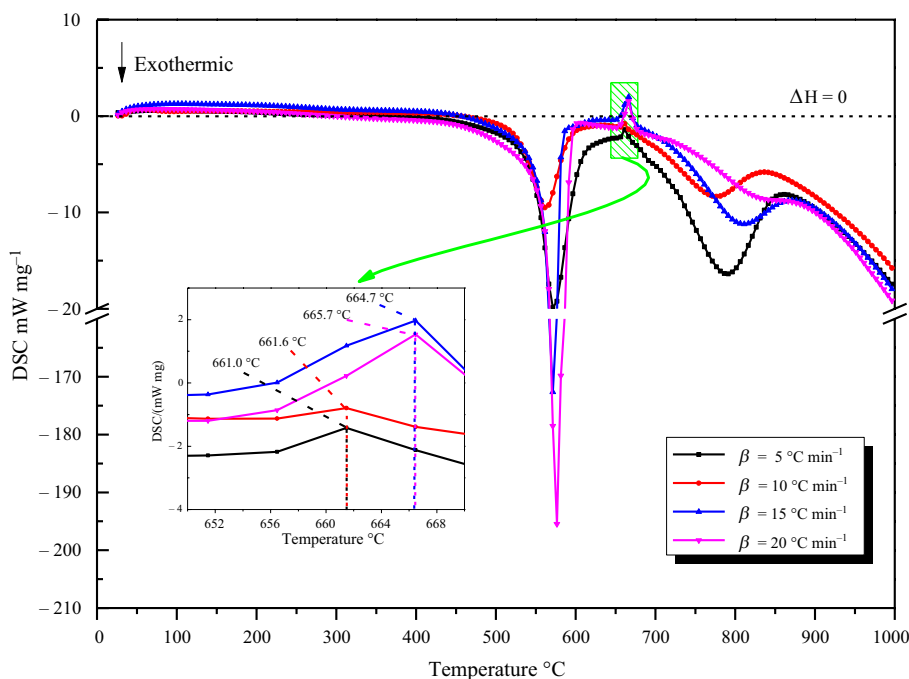


Fig. 10 DTG sub-peak curves of NAP at stage IV

Fig. 11 DSC curves of NAP at multiple heating rates**Table 4** Mass gain at four heating rates of 5, 10, 15, and 20 °C min⁻¹ at different stages (%)

Stage	Δm	5/°C min ⁻¹	10/°C min ⁻¹	15/°C min ⁻¹	20/°C min ⁻¹
I	Δm_1	4.5	5.78	5.92	6.17
II	Δm_2	24.63	23.24	23.62	35.79
III	Δm_3	0.88	0.6	0.23	0
IV	Δm_4	36.74	36.13	23.61	9.59

was. Moreover, as the heating rate increased, the peak temperature was gradually increased [21]. At the heating rate of 5, 10, 15, and 20 °C min⁻¹, T_p was 561.3, 572.0, 567.9, and 572.4 °C, respectively. Hysteresis occurred because some amorphous alumina could not be converted in time, and the crystalline oxide drifted to a high temperature. However, this had little effect on the sub-peak value [26]. As shown in Fig. 10, the values of the sub-peak were between 0.98% and 3.03% min⁻¹ for different heating rates.

Figure 11 delineates the variation among heat outputs of the NAP with the temperature at multiple heating rates. The DSC curves fell sharply at 550–600 °C. The NAP oxidized rapidly and released considerable amounts of heat. The thermal release of the NAP differed at multiple heating rates [21]. The thermal released was 35,126, 27,955, 15,608, and 16,336 J g⁻¹ at heating rates of 5, 10, 15, and 20 °C min⁻¹, respectively.

The heat absorption of the DSC curve was different in the solid aluminum melting stage of the NAP at multiple heating rates. As presented in Table 3, the melting temperature of

the NAP was 661.0, 661.6, 664.7, and 665.7 °C for 5, 10, 15, and 20 °C min⁻¹ heating rates, respectively. The temperature was approximately 660 °C, which is the melting point of aluminum powders. For solid aluminum to melt into liquid aluminum, it must gain heat. However, an oxidation reaction causes it to lose heat. The two reactions cannot be separated from each other and did partly overlap. Therefore, the endothermic effect of the aluminum powders was not obvious.

Kinetic characteristics

With a fixed heating rate, the mechanism functions in Table 2 were introduced into Eq. 7 and 9, respectively. The kinetic parameters of apparent activation energy (E , J mol⁻¹) and pre-exponential factor (A , min⁻¹) were calculated using the Satava-Sestak and Ozawa method, respectively.

Compared with E_s obtained by Satava-Sestak method and E_o obtained by Ozawa method, apparent activation energy was obtained when meeting the following conditions:

$$|(E_o - E_s)/E_o| \leq 0.1$$

Correspondingly, the mechanism function was also obtained. According to Arrhenius equation in Eq. 11, the reaction rate constant (k) was obtained:

$$k = A \exp(-E/RT) \quad (11)$$

The kinetic parameters of thermal oxidation of NAP are listed in Table 5. E characterizes the ease of oxidation reaction. The smaller the E is, the easier the reaction occurs [31]. The E was 875.12, 1556.80, 5701.00,

Table 5 Kinetic parameters of NAP

$\beta/^\circ\text{C min}^{-1}$	A/min^{-1}	$E/\text{J mol}^{-1}$	k	R^2
5	19.31	875.12	$19.31\exp(-105.26/T)$	0.92537
10	24.93	1556.80	$24.93\exp(-187.25/T)$	0.98293
15	26.01	5701.00	$26.01\exp(-685.71/T)$	0.94386
20	49.63	9739.21	$49.63\exp(-1171.42/T)$	0.98377

and 9739.21 J mol⁻¹ at heating rates of 5, 10, 15, and 20 °C min⁻¹, respectively. Therefore, the average E (\bar{E}) was 4468.03 J mol⁻¹. Furthermore, A was 19.31, 24.93, 26.01, and 49.63 min⁻¹ at heating rates of 5, 10, 15, and 20 °C min⁻¹, respectively. Thus, the average A (\bar{A}) was 29.97 min⁻¹. Under the same conditions, the smaller the heating rate was, the easier the oxidation reaction occurred.

The non-isothermal oxidation of NAP conformed to the number 29 contraction ball (volume) function model. The most probable mechanism function was $G(\alpha) = 1 - (1 - \alpha)^{1/3}$.

Conclusions

The dynamic oxidation process of NAP can be divided into initial oxidation (I), severe oxidation (II), solid aluminum melting (III), and secondary oxidation (IV) in the temperature range from 30 to 1000 °C. The path of polymorphic phase transformations of aluminum was amorphous $\rightarrow \gamma \rightarrow \alpha\text{-Al}_2\text{O}_3$ in the dynamic oxidation process.

The heating rate has a considerable effect on the oxidation process of NAP. The mass gain was mainly concentrated at stages II and IV. As the heating rate increased, the mass gain reduced in stage II and increased in stage IV. The mass gain rate was 2.38, 4.7, 33.79, and 53.38% min⁻¹ at 5, 10, 15, and 20 °C min⁻¹, respectively. The thermal release was 35,126, 27,955, 15,608, and 16,336 J g⁻¹ at 5, 10, 15, and 20 °C min⁻¹, respectively.

Based on the kinetic integral method, \bar{E} and \bar{A} were calculated as 4468.03 J mol⁻¹ and 29.97 min⁻¹. The non-isothermal oxidation of NAP conformed to the number 29 mechanism function.

Acknowledgements The authors gratefully acknowledge financial support by National Key Research and Development Program of China (No. 2021YFB4000905), National Natural Science Foundation of China (No. 52104214), and the Youth Innovation Team of Shaanxi Universities, China (No. 22JP049).

References

- Meda L, Marra G, Galfetti L, Severini F, Luca LD. Nano-aluminum as energetic material for rocket propellants. *Mater Sci Eng.* 2007;27:1393–6.
- Pourmortazavi SM, Hajimirsadeghi SS, Kohsari I, Fathollahi M, Hosseini SG. Thermal decomposition of pyrotechnic mixtures containing either aluminum or magnesium powder as fuel. *Fuel.* 2008;87:244–51.
- Marmo L, Piccinini N, Danzi E. Small magnitude explosion of aluminium powder in an abatement plant: a telling case. *Process Saf Environ Prot.* 2015;98:221–30.
- Li G, Yang HX, Yuan CM, Eckhoff RK. A catastrophic aluminium-alloy dust explosion in china. *J Loss Prevent Proc.* 2016;39:121–30.
- Deng J, Qu J, Wang QH, Zhai XW, Xiao Y, Cheng Y, Shu CM. Minimum ignition temperature of aluminium dust clouds via the Godbert-Greenwald furnace. *Process Saf Environ Prot.* 2019;129:176–83.
- Li QZ, Lin BQ, Li WX, Zhai C, Zhu CJ. Explosion characteristics of nano-aluminum powder–air mixtures in 20 L spherical vessels. *Powder Technol.* 2011;212:303–9.
- Bernard S, Gillard P, Frascati F. Ignition and explosibility of aluminium alloys used in additive layer manufacturing. *J Loss Prevent Proc.* 2017;49:888–95.
- Wu HC, Ou HJ, Peng DJ, Hsiao HC, Gau CY, Shih TS. Dust explosion characteristics of agglomerated 35 nm and 100 nm aluminum particles. *Int J Chem Eng.* 2010;9:1–6.
- Wu HC, Ou HJ, Hsiao HC, Shih TS. Explosion characteristics of aluminum nanopowders. *Aerosol Air Qual Res.* 2010;10:38–42.
- Denkevits A, Hoess B. Hybrid H₂/Al dust explosions in Siwek sphere. *J Loss Prevent Proc.* 2015;36:509–21.
- Liu XL, Zhang Q. Influence of turbulent flow on the explosion parameters of micro- and nano-aluminum powder–air mixtures. *J Hazard Mater.* 2015;299:603–17.
- Zhang Q, Liu LJ, Shen SL. Effect of turbulence on explosion of aluminum dust at various concentrations in air. *Powder Technol.* 2018;325:467–75.
- Castellanos D, Carreto-Vazquez VH, Mashuga CV, Trottier R, Mejia AF, Mannan MS. The effect of particle size polydispersity on the explosibility characteristics of aluminum dust. *Powder Technol.* 2014;254:331–7.
- Huang Y, Risha GA, Yang V, Yetter RA. Combustion of bimodal nano/micron-sized aluminum particle dust in air. *Proc Combust Inst.* 2007;31:2001–9.
- Yuasa S, Sogo S, Isoda H. Ignition and combustion of aluminum in carbon dioxide streams. *Symp Combust.* 1992;24:1817–25.
- Bidabadi M, Moallemi N, Shabani A, Abdous MA. Analysis of size distribution and ignition temperature effects on flame speeds in aluminium dust clouds. *J Aerosp Eng.* 2010;224:113–9.
- Zhu Y, Yuasa S. Effects of oxygen concentration on combustion of aluminum in oxygen/nitrogen mixture streams. *Combust Flame.* 1998;115:327–34.
- Li LB, Chen X, Musa O, Zhou CS, Zhu M. The effect of pressure and oxygen concentration on the ignition and combustion of aluminum–magnesium fuel–rich propellant. *Aerosp Sci Technol.* 2018;76:394–401.
- Gao W, Zhang XY, Zhang DW, Peng QK, Zhang Q, Dobashi R. Flame propagation behaviours in nano-metal dust explosions. *Powder Technol.* 2017;321:154–62.
- Qu J, Deng J, Luo ZM, Xiao Y, Shu C-M. Thermal reaction characteristics and microstructure evolution of aluminium nanopowder in various mixtures of oxygen and nitrogen atmosphere. *Process Saf Environ Prot.* 2023;170:45–53.

21. Tseng JM, Huang ST, Duh YS, Hsieh TY, Sun YY, Lin JZ, et al. Thermal analysis and safety information for metal nanopowders by DSC. *Thermochim Acta*. 2013;566:257–60.
22. Zhu BZ, Wang Q, Sun YL, Jia T. Thermal reaction characterization of micron-sized aluminum powders in CO₂. *Russ J Phys Chem*. 2016;10:644–50.
23. Johnson CE, Fallis S, Chafin AP, Groshens TJ, Higa KT. Characterization of nanometer- to micron-sized aluminum powders: Size distribution from thermogravimetric analysis. *J Propul Power*. 2007;23:669–82.
24. Vlaskin MS, Shkolnikov EI, Bersh AV. Oxidation kinetics of micron-sized aluminum powder in high-temperature boiling water. *Int J Hydrogen Energy*. 2011;36:6484–95.
25. Feng JQ, Hays DA. Relative importance of electrostatic forces on powder particles. *Powder Technol*. 2003;135:65–75.
26. Hu B, Yi Y, Liang C, Yuan ZL, Szczepan R, Yang LJ. Experimental study on particles agglomeration by chemical and turbulent agglomeration before electrostatic precipitators. *Powder Technol*. 2018;335:186–94.
27. Hu RZ, Gao SL, Zhao FQ, et al. Thermal analysis kinetics. 2nd ed. Science Press; 2008.
28. Rufino B, Coulet MV, Bouchet R, Isnard O, Denoyel R. Structural changes and thermal properties of aluminium micro- and nanopowders. *Acta Mater*. 2010;58:4224–32.
29. Sun J, Simon SL. The melting behavior of aluminum nanoparticles. *Thermochim Acta*. 2007;463:32–40.
30. Schoenitz M, Patel B, Agboh O, Dreizin EL. Oxidation of aluminum powders at high heating rates. *Thermochim Acta*. 2010;507:115–22.
31. Jones DEG, Brousseau P, Fouchard RC, Turcotte AM, Kwok QSM. Thermal characterization of passivated nanometer size aluminium powders. *J Therm Anal Calorim*. 2000;61:805–18.
32. Sun YL, Sun R, Zhu BZ, Mao KK, Wu YX. Thermal reaction mechanisms of nano- and micro- scale aluminum powders in carbon dioxide at low heating rate. *J Therm Anal Calorim*. 2016;124:1727–34.
33. Hasani S, Panjepour M, Shamanian M. Non-isothermal kinetic analysis of oxidation of pure aluminium powder particles. *Oxid Met*. 2013;81:299–313.
34. Zeng W, Liu JC, Chen XX, Ma HA. A new reduced reaction mechanism of a surrogate fuel for kerosene. *Can J Chem Eng*. 2013;91:483–9.
35. Tognotti L, Malotti A, Petarca L, Zanelli S. Measurement of Ignition Temperature of Coal Particles Using a Thermogravimetric Technique. *Combust Sci Tech*. 1985;44:15–28.
36. Trunov MA, Schoenitz M, Zhu XY, Dreizin EL. Effect of polymorphic phase transformations in Al₂O₃ film on oxidation kinetics of aluminum powders. *Combust Flame*. 2005;140:310–8.
37. Trunov MA, Schoenitz M, Dreizin EL. Effect of polymorphic phase transformations in alumina layer on ignition of aluminum particles. *Combust Theor Model*. 2006;10:603–24.
38. Rai A, Park K, Zhou L, Zachariah MR. Understanding the mechanism of aluminum nanoparticle oxidation. *Combust Theor Model*. 2006;10:843–59.
39. Hasani S, Panjepour M, Shamanian M. The oxidation mechanism of pure aluminium powder particles. *Oxid Met*. 2012;78:179–95.

Publisher's Note Springer Nature remains neutral with regard to jurisdictional claims in published maps and institutional affiliations.

Springer Nature or its licensor (e.g. a society or other partner) holds exclusive rights to this article under a publishing agreement with the author(s) or other rightsholder(s); author self-archiving of the accepted manuscript version of this article is solely governed by the terms of such publishing agreement and applicable law.